# Open Research Online

## Modeling the Martian dust cycle 1. Representations of dust transport processes

## Journal Item

For guidance on citations see FAQs.

Version: [not recorded]

Link(s) to article on publisher's website:
http://dx.doi.org/doi:10.1029/2002JE001910
http://www.agu.org/journals/je/je0212/2002JE001910/2002JE001910.pdf

# oro.open.ac.uk

# Modeling the Martian dust cycle. 1: Representations of dust transport processes

**Claire E. Newman, Stephen R. Lewis, and Peter L. Read**

Atmospheric, Oceanic and Planetary Physics, Department of Physics, Oxford University, Oxford, England

**François Forget**

Laboratoire de Météorologie Dynamique du CNRS, Université Paris 6, Paris

### Abstract

A dust transport scheme has been developed for a general circulation model of the Martian atmosphere. This enables radiatively active dust transport, with the atmospheric state responding to changes in the dust distribution via atmospheric heating, as well as dust transport being determined by atmospheric conditions. The scheme includes dust lifting, advection by model winds, atmospheric mixing, and gravitational sedimentation. Parameterizations of lifting initiated by a) near-surface wind stress and b) convective vortices known as dust devils are considered. Two parameterizations are defined for each mechanism, and are first investigated offline using data previously output from the non-dust transporting model. The threshold-insensitive parameterizations predict some lifting over most regions, varying smoothly in space and time. The threshold-sensitive parameterizations predict lifting only during extreme atmospheric conditions (such as exceptionally strong winds) so lifting is rarer and more confined to specific regions and times. Wind stress lifting is predicted to peak during southern summer, largely between latitudes 15°– 35°S, with maxima also in regions of strong slope winds or thermal contrast flows. These areas are consistent with observed storm onset regions and dark streak surface features. Dust devil lifting is also predicted to peak during southern summer, with a moderate peak during northern summer. The greatest dust devil lifting occurs in early afternoon, particularly in the Noachis, Arcadia/Amazonis, Sirenum and Thaumasia regions. Radiatively active dust transport experiments reveal strong positive feedbacks on lifting by near-surface wind stress, and negative feedbacks on lifting by dust devils.

## 1 Introduction

Martian atmospheric dust strongly absorbs and scatters short-wave solar radiation, and also absorbs long-wave radiation, resulting in a considerable impact on radiative heating and the thermal and dynamical state of the atmosphere. The potential for large quantities of dust to appear in some regions, in only a broadly predictable manner, therefore makes it a major

Table 1: Seasons, $L_s$ and time of year

| Season | Range in $°L_s$ | Description |
|:------:|:---------------:|:-----------:|
| 1  | 0 – 30    | NH spring  |
| 2  | 30 – 60   |            |
| 3  | 60 – 90   |            |
| 4  | 90 – 120  | NH summer  |
| 5  | 120 – 150 |            |
| 6  | 150 – 180 |            |
| 7  | 180 – 210 | NH autumn  |
| 8  | 210 – 240 |            |
| 9  | 240 – 270 |            |
| 10 | 270 – 300 | NH winter  |
| 11 | 300 – 330 |            |
| 12 | 330 – 360 |            |

contributor to atmospheric variability on Mars, and a good representation of the observed dust cycle is an important component of any model intended to recreate the observed behavior of the atmospheric circulation. The Mars general circulation model used in this work has been developed at the sub-Department of Atmospheric, Oceanic and Planetary Physics at the University of Oxford (AOPP) and at the Laboratoire de Météorologie Dynamique du CNRS in Paris (LMD). The MGCM referred to below is specifically the AOPP version described in *Forget et al.* [1999], and the DMGCM is the MGCM with dust transport included.

For descriptive purposes here the Mars year is split into twelve 'seasons', equally spaced in areocentric longitude $L_s$, as shown in Table 1. The current understanding of the Martian dust cycle and storm occurrence patterns has been reviewed by e.g. *Martin and Zurek* [1993], *McKim* [1996]. Away from southern spring and summer (i.e., $330° < L_s < 360°$ or $L_s < 180°$, seasons 12–6), the global dust load is quite low, with total visible opacities, $\tau_{\text{vis}}$, less than $\sim$0.4. Exceptions occur only when a large dust storm is still to dissipate fully by $L_s \sim 330°$ or when one occurs anomalously early. On a local scale opacities are often higher during this period, e.g. around the retreating polar caps during spring. Opacities then increase during the 'storm season' (a period containing most historically observed large dust storms, from $L_s \sim 180°$–330°, seasons 7–11), owing to increased dust lifting. There is generally at least one distinct peak in dust loading in this period, which also has the greatest interannual variability in dust loading and the maximum zonally-averaged visible opacities each year (typically with $\tau_{\text{vis}} \sim 2$–5).

Large dust storms are important in determining the evolution of opacity. Global or planet-

encircling storms have all been observed to occur at $L_s\sim250°\pm60°$ which is near perihelion at $L_s \sim251°$ and southern summer solstice at $L_s =270°$. The peak in storm activity during the storm season generally occurs within a zonal collar from $\sim20°$–50°S, with initial dust clouds usually found in the southern hemisphere in areas such as Hellas, Argyre and Solis. Regional storms have been observed in almost every Mars year for which there are data. Such storms could well be ubiquitous in southern spring to summer, but viewing restrictions for Earth-based observations apply in most years.

The effect of atmospheric dust in a Mars general circulation model is often represented by allowing the radiation scheme to respond to a prescribed three-dimensional, time varying dust distribution, which is structured to represent some sort of 'typical' Mars year. Section 2 begins with a brief description of the MGCM and some prescribed dust distributions which have been used with it, but this approach, while useful, does have certain drawbacks. Firstly, it is necessary to decide *a priori* which sort of Mars year is to be considered. Secondly, there is no opportunity to assess the interaction between the dust distribution and the atmospheric circulation, since the former cannot vary except in a prescribed fashion. Finally, such a model is missing what may be a vital component for contributing to atmospheric interannual variability.

For these reasons the DMGCM has been developed by adding a dust transport scheme to the MGCM. This allows the dust distribution to vary in response to changes in the atmospheric state, which affect transport processes within the atmosphere and predicted lifting from and deposition to the surface. If the DMGCM is run with radiatively active dust transport the atmosphere also responds to changes in the dust distribution, which affect atmospheric radiative heating. The DMGCM may also be run with passive dust transport – in this case the dust distribution held in the dust transport scheme varies in response to atmospheric transport processes, dust lifting and deposition, but the MGCM continues to use a prescribed dust distribution in its radiation scheme, thus preventing any feedbacks. The second half of section 2 describes most components of the dust transport scheme, in particular giving details of the vertical diffusion scheme and its importance to dust transport within the lower atmosphere. Section 3 consists of a detailed description of how the final component, dust lifting, is parameterized in the DMGCM.

The DMGCM is capable of performing simulations with radiatively active dust transport and parameterized dust lifting. Both atmospheric transport and dust lifting are therefore consistent with the atmospheric state. This means that dust lifting mechanisms can be properly assessed by examining the realism of the dust cycles and atmospheric responses produced and, importantly, that the onset and decay of dust storms in such simulations is truly spontaneous, being determined by the atmospheric state and lifting parameters only. Other Mars general circulation models have also been used to investigate dust transport in the Martian atmosphere. The LMD Mars general circulation model, which has a similar

structure to that of the DMGCM (see section 2), is also capable of performing simulations with radiatively active dust transport and parameterized dust lifting (*Forget et al.* [1998b]). The NASA Ames Mars general circulation model has been coupled to a separate tracer transport model to perform three-dimensional simulations of global dust storms with particle size-dependent, radiatively active dust transport (*Murphy et al.* [1995]). Their experiments mostly used prescribed dust lifting to produce storms, but more recently they have used the model to look at the dust cycles produced using a simple lifting parameterization with radiatively active dust transport (*Murphy* [1999]). The GFDL Mars general circulation model (*Wilson and Hamilton* [1996]) has been used to study dust storms with an emphasis on the atmospheric response to changes in the dust distribution, using prescribed lifting to simulate storm events (e.g. *Wilson* [1997]), or using lifting based on atmospheric stability (*Richardson and Wilson* [2002]).

Section 4 presents the results of preliminary experiments to investigate the dust lifting parameterizations. These use offline data from the MGCM, thus precluding any feedbacks between the MGCM and dust transport and thereby simplifying the analysis. Some attempt is made, however, to assess the likely direction of any dust lifting feedbacks, and results of DMGCM radiatively active dust transport simulations are shown as confirmation in section 5. Experiments in which the DMGCM is run continuously for a number of years, with parameterized dust lifting and radiatively active dust transport, are presented and discussed in a companion paper (*Newman et al.* [2002]).

## 2  The Mars general circulation model and dust transport scheme

Mars general circulation models have been developed jointly at AOPP and LMD since 1993. The MGCM is the AOPP version of the AOPP-LMD Mars general circulation model described fully in *Forget et al.* [1999], and uses a spectral representation of dynamical fields. The MGCM consists of a dynamical core, which for these experiments is called 480 times per sol, and parameterizations of physical processes, including radiative transfer, which are called after every tenth dynamics time-step. For this discussion the most important aspect of the MGCM is the parameterization of dust radiative effects.

The scattering of thermal infrared radiation by dust is accounted for in wide wavelength bands outside the $CO_2$ 15$\mu$m band, using a multiple scattering method based on the work of *Toon et al.* [1989]. The wavelength-integrated mean single scattering properties (extinction coefficient $\bar{Q}_{ext}$, single scattering albedo $\bar{\omega}$ and asymmetry parameter $\bar{g}$) are derived from spectral properties calculated as described by *Forget* [1998a]. These properties are similar to those used by *Toon et al.* [1977], but are modified such that simulated spectra are better able to duplicate, at all wavelengths, spectra obtained in 1971 by the Infrared Interferometer Spectrometer on the Mariner 9 spacecraft. Absorption of thermal infrared radiation by

dust in the $CO_2$ 15$\mu$m band is added to that by $CO_2$, using a mean absorption parameter $\bar{Q}_{abs} = (1 - \bar{\omega})\bar{Q}_{ext}$. The scattering and absorption of solar radiation is modeled by using the delta-Eddington approximation (see e.g. *Joseph et al.* [1976]) to compute reflectances and transmittances of atmospheric layers, then finding the radiation fluxes. The calculations are performed using spectrally-averaged dust properties, derived by *Clancy and Lee* [1991] from Viking Orbiter Infrared Thermal Mapper emission-phase-function measurements, in two broad wavelength bands (0.1–0.5$\mu$m and 0.5–5$\mu$m).

The radiation scheme then requires the optical depth of dust within each atmospheric layer to finally calculate the radiation fluxes and hence the net heating caused by a given dust distribution. In the MGCM a number of prescribed dust distributions have been used within the radiation scheme to represent different types of Mars years (*Lewis et al.* [1999]). The 'low dust' scenario sets the visible dust opacity at all times and locations to 0.1, with a dust top of about 30km (this being the altitude above which dust mixing ratios decrease very rapidly). The 'Viking dust' scenario is modeled on that observed during the Viking Lander years (see e.g. *Zurek and Martin* [1993]) but with the large dust storm peaks removed. In this scenario the dust top is highest over the equator during the storm season, lowest over the poles, and $\tau_{vis}$ peaks at 1 during the storm season. Two further 'dust storm' scenarios, ds2 and ds5, have respectively two and five times more dust at each grid-point than the Viking scenario but are otherwise identical.

The dust transport scheme consists of dust lifting into the atmosphere, atmospheric advection and mixing, and sedimentation under gravity, including deposition to the surface. Most of these parameterizations are described below, although the whole of section 3 is devoted to the larger topic of parameterizing dust lifting. For simplicity a single particle size of 2$\mu$m in diameter is used in the dust transport scheme, affecting sedimentation rates and some dust lifting predictions. This choice is roughly consistent with observational estimates of the dominant particle sizes in the Martian atmosphere (e.g. *Pollack et al.* [1995]). (In the radiation scheme described above, however, the dust radiative properties used are representative of a reasonable particle size distribution rather than 2$\mu$m particles.)

Advection is conducted by a semi-Lagrangian material advection scheme (similar to the scheme of *Williamson and Rasch* [1989]), which uses the method of *Priestley* [1993] to add monotonicity constraints and conserve mass (as semi-Lagrangian schemes are not inherently conservative). The advection scheme uses winds output from the MGCM during each call to physics (i.e., 48 times per sol) and has the same layout and resolution as the model physics grid (5° longitude by 5° latitude with 25 vertical levels for these experiments).

Gravitational sedimentation is modeled by calculating the fall velocity for a given size of dust particle, and using this in a one-dimensional Van Leer I advection scheme (*Hourdin and Armengaud* [1997]) which uses a finite volume approach to ensure mass conservation. The fall velocity is found by equating the buoyancy-adjusted downward gravitational force and

the upward drag force (due to friction between the falling particles and the atmosphere, given by Stokes's Law), with the Cunningham 'slip-flow' correction used to allow for the rarefied nature of the Martian atmosphere (*Rossow* [1978]). Sedimentation in the lower atmosphere results in particles falling out to the surface.

Convective adjustment is required if the temperature lapse rate becomes super-adiabatic. The scheme is designed to restore the adiabatic profile $\bar{\theta}$ from the initial profile $\theta$. In the real atmosphere this takes place on scales far smaller than the model grid size, but the dust transport scheme makes the adjustment to dust mixing ratios on grid scales using the same energy-conserving convective adjustment scheme used for momentum in the MGCM (*Hourdin et al.* [1993]). In this scheme the mixing intensity then depends on the intensity of the convection.

The vertical diffusion scheme deals with the transport of dust by small-scale turbulence (on scales smaller than the model grid), particularly in the planetary boundary layer. This may be parameterized using the classical diffusion equation, and in the dust transport scheme the vertical mixing of a variable $a$ is computed as

$$\frac{\partial a}{\partial t} = \frac{1}{\rho} \left( \frac{\partial}{\partial z} K \rho \frac{\partial a}{\partial z} \right) \tag{1}$$

where $\rho$ is atmospheric density. $K$ takes different values for the horizontal wind components and for potential temperature and dust, and these values are calculated using a modified version of the 2.5 level scheme of *Mellor and Yamada* [1982] (see *Forget et al.* [1999] for more details of the coefficients used).

If the DMGCM is first run without convective adjustment or vertical diffusion in the dust transport scheme, dust is unable to penetrate above an altitude of a few hundred meters, except at very small fractions of the initial amount injected. The dust is, effectively, trapped due to the rapidity of gravitational sedimentation back to the surface. A similar result is obtained if convective adjustment is included, but when vertical diffusion is included the dust is carried rapidly up into the main section of the atmosphere by vertical mixing. In the DMGCM, convective adjustment is of secondary importance to vertical diffusion in producing atmospheric mixing, and only a small difference is found between results of similar experiments performed with vertical diffusion but with and without convective adjustment. The dependence of dust transport, in the DMGCM boundary layer, on vertical diffusion also means that results may be affected by the exact vertical diffusion scheme or vertical diffusion coefficients used.

# 3 Parameterizations of dust lifting

## 3.1 Lifting by near-surface wind stress

### 3.1.1 The basic theory

The loose surface material on Mars may be classified into two types in terms of behavior: sand and dust particles. 'Sand' is defined as particles which move in saltation. These particles may be raised from the surface by high winds, but are simply too heavy to remain suspended and therefore return quite rapidly to the surface, having never become part of the full atmospheric circulation. On Mars such particles are generally $\geq 20\mu$m in diameter. 'Dust' is defined as particles which can go into suspension. The background vertical wind velocity plus the turbulent effects of the wind may be sufficient to keep them aloft, against the downward pull of gravity, once they have been lifted from the surface, and they will therefore probably be carried into the full circulation, although larger dust particles in particular may fall out at some later time.

One possible mechanism for the injection of dust particles into the atmosphere is lifting by near-surface wind stress. *Bagnold* [1954] noted that two thresholds may be defined regarding this method of lifting particles from a surface: the fluid threshold and the impact threshold. The former is the point at which wind stress alone is large enough to lift particles from the surface. The situation is generally represented by defining a threshold drag velocity, $u_{\mathrm{drag}}^{\mathrm{t}}$, which must be exceeded by the actual drag velocity, $u_{\mathrm{drag}}$, for lifting to occur. $u_{\mathrm{drag}}$ relates to near-surface wind stress, $\zeta$, and atmospheric density via

$$u_{\mathrm{drag}} = \sqrt{\frac{\zeta}{\rho}}, \tag{2}$$

and may be determined from near-surface wind velocities in the surface boundary layer (see e.g. *Garratt* [1994]). All velocity components are close to zero in a very thin layer next to the ground (approximately $\frac{1}{30}$ the diameter of typical surface particles), and just above this is a sub-layer within which velocities vary approximately logarithmically with height, i.e.,

$$u(z) \simeq \frac{u_{\mathrm{drag}}}{k} \ln\left(\frac{z}{z_0}\right). \tag{3}$$

Here $k$ is von Karman's constant, taken =0.4, $z$ is height above the surface and $z_0$ is the height at which velocities go to zero (called the roughness height). In the dust transport scheme, $z_0$ is taken as 0.01m everywhere, within the 0.001-0.01m range estimated by *Sutton et al.* [1978] for the Viking lander sites. Therefore

$$u_{\text{drag}} = \frac{ku(z)}{\ln\left(\frac{z}{z_0}\right)}. \tag{4}$$

Many experiments have been performed to find a semi-empirical equation for $u_{\text{drag}}^{\text{t}}$, for conditions appropriate to both the Earth and other planets (*Bagnold* [1954], *Greeley and Iversen* [1985]). It may be written in the general form

$$u_{\text{drag}}^{\text{t}} = A\sqrt{gD_{\text{p}}\frac{\rho_{\text{d}} - \rho}{\rho}}, \tag{5}$$

where $\rho_{\text{d}}$ is the density of the material from which dust particles are constituted, $\sim 2700$ kgm$^{-3}$, and $D_{\text{p}}$ is the particle diameter in meters. This encapsulates the general idea that heavier (in this case, larger) particles are harder to lift, but important details are concealed by the factor $A$. A semi-empirical formula set often used to predict $A$ (e.g. *Greeley and Iversen* [1985], *Lorenz et al.* [1995]), is given below, and these equations must be solved iteratively:

$$A = 0.2\left(1 + I_{\text{p}}/\rho_{\text{d}}gD_{\text{p}}^{2.5}\right)^{0.5}/(1 + 2.5R_{*\text{t}})^{0.5}, \tag{6}$$

if $0.03 < R_{*\text{t}} < 0.3$,

$$A = 0.129\left(1 + I_{\text{p}}/\rho_{\text{d}}gD_{\text{p}}^{2.5}\right)^{0.5}/\left(1.928R_{*\text{t}}^{0.092} - 1\right)^{0.5}, \tag{7}$$

if $0.3 < R_{*\text{t}} < 10$,

$$A = 0.120\left(1 + \frac{I_{\text{p}}}{\rho_{\text{d}}gD_{\text{p}}^{2.5}}\right)^{0.5}\{1 - 0.0858e^{-0.0617(R_{*\text{t}}-10)}\}, \tag{8}$$

if $R_{*\text{t}} > 10$,

where $R_{*\text{t}}$ is the friction Reynolds number at threshold $= u_{\text{drag}}^{\text{t}}D_{\text{p}}/\nu$, $\nu$ is the kinematic viscosity ( = dynamic viscosity / density) and $I_{\text{p}}$ is the interparticle cohesion parameter.

Typical plots of $u_{\text{drag}}^{\text{t}}$ versus $D_{\text{p}}$ are shown in Fig. 1 and reveal that, if the interparticle cohesion $I_{\text{p}}$ is greater than zero, $u_{\text{drag}}^{\text{t}}$ varies as $\sim\sqrt{D_{\text{p}}}$ only above a certain diameter. Below this, $u_{\text{drag}}^{\text{t}}$ increases as $D_{\text{p}}$ decreases due to the growing importance of interparticle cohesion effects as the particle size decreases. These make it harder for particles to be removed from the particle bed, and give rise to the minima seen in the plots, corresponding to the optimum balance between weight and cohesion. Interparticle cohesion has not been measured on Mars, but a typical value used for both Earth and Mars is $6\times10^{-7}$Nm$^{-1/2}$ (*Greeley and Iversen*
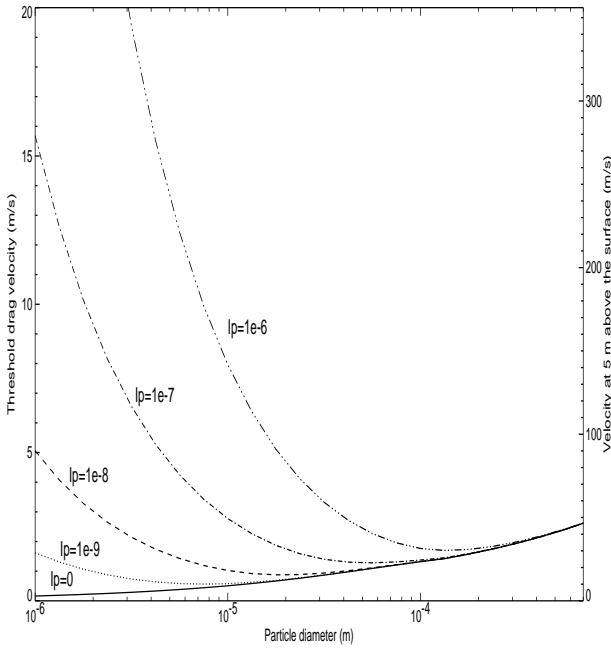
Figure 1: The variation of threshold drag velocity (left-hand axis) and corresponding wind magnitudes at 5m (right-hand axis) with particle diameter at a grid-point in northern Hellas, using interparticle cohesions $I_\mathrm{p}$=0–1×$10^{-6}$Nm$^{-1/2}$.

[1985], *Lorenz et al.* [1995]). A problem with using near-surface wind stress lifting to explain the observed atmospheric dust distribution then arises because, according to this basic theory, the optimum size to be lifted is sand-sized. If $I_\mathrm{p} \simeq 6\times10^{-7}$Nm$^{-1/2}$ the optimum size is about $90\mu$m in diameter. By contrast, the predominant particle size in the atmosphere is estimated to be of order $1\mu$m (e.g. *Toon et al.* [1977], *Pollack et al.* [1995]), and such small particles appear, from Fig. 1, to require unfeasibly high surface winds, or extremely low interparticle cohesions, for lifting to occur.

The above results suggest that dust is not lifted from the surface of Mars by near-surface wind stress, but observations indicate otherwise, in particular dark wind streaks which are probably caused by the removal of bright dust from a darker underlying surface. During well observed dust storms, peak dust opacities have often been strongly correlated with fast-moving fronts, also seeming to indicate that dust is being raised by these high winds (e.g. *James and Evans* [1981]).

### 3.1.2   The effect of saltation

*Pollack et al.* [1976] and others have suggested that, if wind speeds on Mars are indeed well below the fluid threshold for dust particles, dust may be raised via saltation of sand particles. Consider a situation where near-surface winds are less than the fluid threshold for dust lifting, but large enough to overcome the fluid threshold for sand. The sand particles saltate back to the surface, adding to the surface stress, and dust lifting occurs if the total surface stress exceeds the dust fluid threshold. The magnitude of the near-surface wind stress contribution to the total is then defined as the impact threshold, since it is the minimum wind stress required for dust lifting in the presence of impacting (saltating) particles.

The amount of dust lifted in the presence of saltation is generally set proportional to the saltation flux. By estimating the forces on surface material in the presence of both wind stress and saltation, Bagnold was able to construct part of a formula to give the vertically-integrated horizontal sand particle flux $H$, and the modified form given below is due to *White* [1979]. From momentum arguments, and also from experimental experience, White suggested that $H$ (in $kgm^{-1}s^{-1}$) could be given by

$$H = \max\left[0,\ 2.61\frac{\rho}{g}\left(u_{\mathrm{drag}}\right)^3\left(1 - \frac{u_{\mathrm{drag}}^{\mathrm{t}}}{u_{\mathrm{drag}}}\right)\left(1 + \frac{u_{\mathrm{drag}}^{\mathrm{t}}}{u_{\mathrm{drag}}}\right)^2\right]. \tag{9}$$

The vertical flux $V_{\mathrm{N}}$ of particles lifted into suspension (dust particles) by the near-surface wind stress mechanism is then assumed to be roughly proportional to this horizontal flux, (again based on observational evidence), giving

$$V_{\mathrm{N}} = \alpha_N H, \tag{10}$$

where the constant of proportionality, $\alpha_N$, is the near-surface wind stress 'lifting efficiency'. The near-surface wind stress lifting parameterizations used in section 4.1 assume that saltation is necessary for the raising of dust particles. The method is as follows: the fluid threshold drag velocity is calculated for the optimum (i.e. sand-sized) particle size, and whenever this is exceeded the vertical dust flux is set proportional to the estimated sand flux, using Eqns. 9 and 10. $\alpha_N$ is, in practice, an unknown parameter, which must be tuned to produce the desired range of dust opacities in a full model simulation. Briefly, the tuning process requires a new simulation, lasting up to one Mars year, to be performed whenever the predicted thresholds are changed (e.g., by altering the interparticle cohesion parameter used to calculate them). The spatial and temporal variation in atmospheric dust opacity produced by this combination of parameters is then compared to that observed, and $\alpha_N$ is adjusted to provide the most realistic result. More care is required for radiatively active dust transport simulations, as the effect of varying $\alpha_N$ is non-linear in the presence of feedbacks.

The above method is a simplification. $\alpha_N$ should, for example, vary with dust particle size, and there is no consideration given as to whether the saltation-enhanced drag velocities would be sufficient to lift dust particles, particularly smaller ones with higher thresholds. To investigate this further, the actual increase in stress due to saltation may be estimated by finding a saltation-modified surface roughness, $z_{0_{salt}}$ (as given by *Raupach* [1991]) and inserting this into Eqn. 4 in place of $z_0$ (e.g. *Gillette et al.* [1998]). Using a low value of $I_p$ ($10^{-8} \mathrm{Nm}^{-1/2}$) to allow saltation at several grid-points, the modification typically gives maximum increases in predicted drag velocities of $\sim 30\%$. This is consistent with wind tunnel observations made under approximately Martian conditions (*Greeley et al.* [1992]), but to lift $2 \mu \mathrm{m}$ diameter particles, for example, would require roughly a 100% increase, even with such a low $I_p$ value. Eqn. 10 is thus overly simplistic, but has the advantage of relative simplicity whilst retaining threshold behavior in predicted dust lifting, and is used in the remainder of this work.

### 3.1.3 Other complications

Several other complications to near-surface wind stress lifting may also be considered, since a slight change in predicted drag velocities and/or thresholds may make the difference between zero and substantial lifting (if $\alpha_N$ is large enough). These fall into two categories – uncertainties in the input data, and modifications to the basic theory.

In the first category are data on interparticle cohesion, $I_p$, roughness height, $z_0$, and the wind gustiness parameter, $\kappa$ (introduced below). $I_p$ has a large potential impact on thresholds, with both the optimum particle size and drag velocity required decreasing as cohesion is reduced (see Fig. 1). This is problematic as there has been no measurement made of $I_p$ on the surface of Mars at even one location, and the same is true of accurate measurements of $z_0$ (with drag velocities reduced over smoother surfaces).

In the second category is the inclusion of saltation and stability effects when calculating the near-surface stress. As discussed above it is clear that, if the interparticle cohesions on Mars are of order $10^{-7} \mathrm{Nm}^{-1/2}$, saltating (i.e., sand) particles appear to have the best chance of being moved, with the added stress due to saltation possibly enough to lift smaller particles. Unstable conditions also lead to increased drag velocities (e.g. *Businger et al.* [1971]) and MGCM data predicts an average increase of between 25% and 40% over all grid-points. The highest drag velocities (those approaching threshold), however, show increases of only $\sim 1\%$, so the impact on dust lifting is likely to be very small. Wind 'gustiness', the variation of wind velocity on short timescales, is another phenomenon which must be considered. The MGCM, like most general circulation models, does not resolve short-lived, small scale waves, eddies or convective events, but rather produces smoothly varying balanced fields, representative of the more slowly varying large- to global-scale components of the atmospheric circulation. MGCM wind velocities, typically output every half an hour, may thus be thought of as

representing the background, slowly-varying winds on Mars, but short timescale variability is not explicitly represented by the model. Actual winds on Mars are distributed about such representative values, depending on the degree of gustiness. So even if the MGCM is able to correctly model the background wind on Mars, a simple 'lift if $u_{\mathrm{drag}} > u_{\mathrm{drag}}^{\mathrm{t}}$' parameterization will fail to capture dust lifting by strong gusts during a period when the mean wind is below threshold. In order to combat this problem the wind distribution may be modeled using a Weibull distribution, such as is used in the terrestrial field of renewable energy (e.g. *Seguro and Lambert* [2000]). Its probability density function,

$$f(v) = (\kappa/c)(v/c)^{\kappa-1} \exp\left[-(v/c)^{\kappa}\right], \qquad (11)$$

leads to a cumulative probability

$$P(< v) = 1 - \exp\left[-(v/c)^{\kappa}\right], \qquad (12)$$

where $v$ is the actual wind speed, $c$ is a scale speed, and $\kappa$ is a dimensionless shape parameter, (with low $\kappa$ values giving longer "tails" of the distribution and hence gustier environments).

*Lorenz et al.* [1995,1996] used Viking Lander hourly-averaged wind speed data, for periods of a few sols at a time, to derive the best fit Weibull distributions. They therefore obtained estimates of $c$ (representative of the typical wind over a few sols) and $\kappa$, the gustiness parameter, which accounts for variations on hourly timescales. The model parameterization, however, requires a gustiness parameter to account for variations on minute timescales. In DMGCM simulations, $c$ is set equal to the drag velocity output every half hour by the MGCM (representative of the typical wind over this period). $\kappa$ has to be smaller (giving more gustiness) than the values obtained from Viking measurements, since more variability (and hence gustiness) is expected when looking at shorter timescales. Hence the range in $\kappa$ of 1–2 found by *Lorenz et al.* [1996] may be taken as an upper limit on the value appropriate for modeling gustiness on minute timescales.

### 3.1.4 Parameterizations of near-surface wind stress lifting

Taking into account these complications to the basic theory, two parameterizations of lifting by near-surface wind stress are investigated more extensively in section 4.1. Both assume saltation to be required before dust lifting occurs, hence thresholds are calculated for sand- (rather than dust-) sized particles, and dust is assumed to be lifted wherever sand is moved.

The first parameterization, denoted GST, then assumes a value of $\kappa=1.5$ to model gustiness effects. The method employed is to integrate, from $u_{\mathrm{drag}}^{\mathrm{t}}$ to, effectively, infinity, Eqn. 9 $\times$ Eqn. 11 (i.e., the estimated sand flux $\times$ the probability density function assumed for $u_{\mathrm{drag}}$), finally multiplying by $\alpha_N$ to give the dust flux. This results in there always being some lifting

everywhere, albeit very little in some cases. The second parameterization, denoted NOG, assumes zero gustiness ($\kappa$ tending to infinity).

These parameterizations of near-surface wind stress dust lifting are more complex than those typically used in Mars general circulation model experiments. *Anderson et al.* [1999], for example, employed White's equation (Eqn. 9) to find the saltation flux for sand transport experiments with the NASA Ames model, but used a constant threshold stress for a given experiment. Earth general circulation models are now placing increasing importance on representing the terrestrial mineral dust cycle, which has a less well known impact on the radiative forcing than the cycle on Mars. Flux relationships similar to those of Eqns. 9 and 10 have typically been used (e.g. *Marticorena and Bergametti* [1995]), but although the same basic formula (Eqn. 5) is usually involved, thresholds are often more directly linked to the soil moisture content (e.g. *Woodward* [2001]) than to the interparticle cohesion $I_p$, and with far more data available for the Earth there is increased use of knowledge regarding particle sizes and types, vegetation cover, etc., within prescribed source regions (see e.g. *Alfaro and Gomes* [2001], *Nickovic et al.* [2001]). The first 3D models which simulated reasonable dust storms (e.g. *Westphal et al.* [1988]) and dust cycles (e.g. *Joussaume* [1990]) have been followed by more sophisticated models which transport a range of particle sizes and types (e.g. *Tegen and Fung* [1994]), and use radiatively active dust transport (e.g. *Nickovic et al.* [2001], *Woodward* [2001]). Less consideration has so far been given to gustiness for Earth-based applications, where dust lifting is a less threshold-limited process, but work has begun on parameterizing the increase in wind velocities due to convective and eddy gusts (e.g. *Lunt* [2001]).

## 3.2   Lifting by dust devils

### 3.2.1   Overview

A dust devil is an atmospheric vortex which may have a vertical scale of up to the height of the convective boundary layer, and a horizontal extent of anywhere from a few centimeters to over a hundred meters. The name dust devil arises because the vortex, with low pressure at its interior and surrounded by high tangential winds and strong vertical velocities (updrafts), is very efficient at sucking in available dust from the surface and raising it to high altitudes within the convective plume (e.g. *Carrol and Ryan* [1970], *Ryan* [1972], *Sinclair* [1973], *Hess and Spillane* [1990]). This process is thought to be far less size-dependent than near-surface wind stress lifting, hence lifting by dust devils may provide an explanation for the occurrence of predominantly $\sim \mu$m dust particles in the Martian atmosphere. Martian dust devils were seen in images taken by the Viking Orbiter cameras (*Thomas and Gierasch* [1985]) and have since been detected and imaged by Mars Pathfinder instruments and found in Mars Global Surveyor Mars Orbiter Camera (MOC) images (e.g. *Metzger and Carr* [1999], *Edgett and*

*Malin* [2000a]).

### 3.2.2 Dust devils as heat engines

*Rennó et al.* [1998] modeled dust devils as convective heat engines, allowing the occurrence and strength of such vortices to be predicted from a knowledge of the atmospheric state, and more recently *Rennó et al.* [2000] have shown that, for candidate dust devil events recorded by Mars Pathfinder lander instruments, the observed wind and pressure fluctuations are consistent with those predicted by the heat engine model. In the model a 'dust devil activity', $\Lambda$, defined as the flux of energy available to drive dust devils, is given by

$$\Lambda \approx \eta F_{\mathrm{s}}, \tag{13}$$

where $\eta$ is the thermodynamic efficiency of the dust devil convective heat engine (the fraction of the input heat which is turned into work), and $F_{\mathrm{s}}$ is the surface sensible heat flux (the heat input to the base of the vortex). $\eta$ increases with the depth of the convective boundary layer, whereas $F_{\mathrm{s}}$ increases with the surface to air temperature gradient, and also has some dependence on surface wind stress.

*Rennó et al.* [1998] showed that $\eta$ may be given approximately by $1 - b$, where

$$b \equiv \frac{(p_{\mathrm{s}}^{\chi+1} - p_{\mathrm{top}}^{\chi+1})}{(p_{\mathrm{s}} - p_{\mathrm{top}})(\chi + 1)p_{\mathrm{s}}^{\chi}} \tag{14}$$

and where $p_{\mathrm{s}}$ is the ambient surface pressure, $p_{\mathrm{top}}$ the ambient pressure at the top of the convective boundary layer, and $\chi$ the specific gas constant divided by the specific heat capacity at constant pressure. In the MGCM, the top of the convective boundary layer is characterized by a rapid drop in turbulent kinetic energy of more than 90% within a few kilometers, with less rapid decay above this critical level. In the dust transport scheme, $p_{\mathrm{top}}$ is therefore defined as the pressure at which the turbulent kinetic energy falls below a critical value of $0.5\mathrm{m}^2\mathrm{s}^{-2}$, this being the value at which decay becomes typically less rapid in the noon and afternoon, tropical and mid-latitude model atmosphere. If a larger critical value of the turbulent kinetic energy is used then the critical level is reached at a lower altitude, hence the convective boundary layer thickness is predicted to be smaller and the amount (and also area, if thresholds are involved) of predicted dust lifting is reduced.

### 3.2.3 Parameterizations of dust devil lifting

In the results presented in section 4.2, dust lifting by dust devils is first estimated by setting it proportional to dust devil activity. In this method, denoted DDA, no threshold for lifting is involved (other than the physical requirement that the lifted dust flux be greater than

zero, which requires the same of the dust devil activity). This results in some dust being lifted by even the weakest vortices predicted, although in reality a minimum amount of lift is surely required (as with the near-surface wind stress parameterization). In DDA the dust flux lifted by the dust devil mechanism, $V_{\mathrm{D}}$, is set equal to $\alpha_D$ times the dust devil activity (where $\alpha_D$ is the dust devil lifting efficiency), i.e.

$$V_{\mathrm{D}} = \alpha_D \Lambda. \tag{15}$$

A second method is then used, which includes the explicit prediction of a threshold for dust devil lifting. Denoted DTH, it is based around work reported by *Greeley and Iversen* [1985], which involved producing dust devils in the laboratory, and finding a semi-empirical formula for the threshold tangential wind speed $v_{\mathrm{tang}}^{\mathrm{t}}$ required to lift a single layer (i.e. one particle thick) of dust from the surface – clearly the minimum for lifting to occur at all. Despite the formulation of the threshold condition in terms of tangential wind speed, dust raising by dust devils is probably due far more to the upward force caused by the pressure drop at the center of the vortex than to enhanced shear stresses at the surface (*Balme et al.* [2001]). $v_{\mathrm{tang}}^{\mathrm{t}}$ was found to be given approximately by

$$v_{\mathrm{tang}}^{\mathrm{t}} = \left(1 + \frac{15}{\rho_{\mathrm{d}} g D_{\mathrm{p}}}\right)^{1/2} \left(\frac{\rho_{\mathrm{d}} g D_{\mathrm{p}}}{\rho}\right)^{1/2}. \tag{16}$$

Having a threshold value for dust lifting, the actual tangential velocity $v_{\mathrm{tang}}$ is required. In order to estimate this the dust devil may be modeled as a steady circular vortex, and cyclostrophic balance used to relate $v_{\mathrm{tang}}$ to the pressure difference across the vortex (from its center to the ambient pressure outside), $\Delta p$. This gives

$$v_{\mathrm{tang}}^2 \approx \frac{\Delta p}{\rho}. \tag{17}$$

The tangential velocity therefore depends on the pressure drop across the dust devil, which is given by the convective heat engine model of *Rennó et al.* [1998] as

$$\Delta p \approx p_{\mathrm{s}} \left\{1 - \exp\left[\left(\frac{\gamma \eta}{\gamma \eta - 1}\right)\left(\frac{\eta_{\mathrm{H}}}{\chi}\right)\right]\right\} \tag{18}$$

where $\gamma$ is the fraction of the total dissipation of mechanical energy consumed by friction at the surface (set to 0.5 in the following experiments) and $\eta_{\mathrm{H}}$ is the horizontal thermodynamic efficiency of the dust devil, given in the dust transport scheme by $(T_{\mathrm{air}} - T_{\mathrm{s}})/T_{\mathrm{s}}$, with $T_{\mathrm{air}}$ the temperature at the lowest model level and $T_{\mathrm{s}}$ the temperature at the surface.

Finally, it is possible to derive a physically justifiable form for the lifted dust flux using this method by extending the theory used to find $v_{\mathrm{tang}}^{\mathrm{t}}$. The threshold value is that required

to lift a single layer, suggesting that, above threshold, the actual tangential velocity could be used to estimate the number of layers, $n$. Using Eqn. 16 gives

$$v_{\text{tang}} = \left(1 + \frac{15}{\rho_{\text{d}} g n D_{\text{p}}}\right)^{1/2} (\rho_{\text{d}} g n D_{\text{p}}/\rho)^{1/2} \tag{19}$$

where, instead of using $n = 1$ to find $v_{\text{tang}}^{\text{t}}$, the calculated tangential velocity, $v_{\text{tang}}$, is used to find $n$. This gives

$$n = \left(\rho v_{\text{tang}}^2 - 15\right)/\rho_{\text{d}} D_{\text{p}} g. \tag{20}$$

The lifted mass per unit area, $\Sigma$, is therefore $n D_{\text{p}} \times \rho_{\text{d}}$ kgm$^{-2}$, which gives

$$\Sigma = \left(\rho v_{\text{tang}}^2 - 15\right)/g \quad \text{kgm}^{-2}. \tag{21}$$

In the DTH parameterization, $\alpha_D$ (the dust devil lifting efficiency) is defined as the rate of lifting by dust devils, therefore the lifted dust flux is given by $V_D = \alpha_D \Sigma$, or

$$V_D = \alpha_D \left(\rho v_{\text{tang}}^2 - 15\right)/g \quad \text{kgm}^{-2}\text{s}^{-1}. \tag{22}$$

As with the near-surface wind stress lifting parameterizations, $\alpha_D$ must be tuned according to the choice of other parameters. In both the DDA and DTH parameterizations, dust is lifted into the lowest model layer (as in GST and NOG). The vertical diffusion scheme raises this dust rapidly through the lower model levels, but a possible modification would be to initially place dust lifted by the dust devil mechanism throughout the boundary layer, representing the rapid upwards transport by these convective vortices.

# 4 Parameterized dust lifting experiments without radiatively active dust transport

The simplest way to begin investigating the parameterizations described above is to look at dust lifting in a DMGCM simulation without radiatively active dust transport. This does not permit the lifted dust to affect the atmospheric state and thus in turn affect future lifting, so enables simpler, more direct analysis. As the interest here is in the predicted dust lifting, rather than in the atmospheric dust distributions which form, however, it is not necessary to run the DMGCM at all. Instead, atmospheric data stored during previous runs of the MGCM are used as input to the lifting parameterizations. These come from the Mars Climate Database (MCD, *Lewis et al.* [1999]), which contains data such as atmospheric temperatures, pressures and winds output by the MGCM using the dust scenarios described in section 2.

The MCD stores seasonal averages at 12 times of sol for each of the twelve seasons defined in Table 1. Such data are ideal to provide spatially resolved estimates of the diurnal and seasonal variation of dust lifting predicted across the planet using each parameterization. Their only drawback is that the seasonal averaging removes extreme values.

## 4.1 Lifting by near-surface wind stress

### 4.1.1 Near-surface wind patterns

Figure 2 demonstrates where peak GST lifting is predicted, and why. The left-hand plots show near-surface drag velocities and wind vectors at ∼5m altitude, in seasons 1, 7 and 10, calculated using Viking dust scenario MCD (i.e. seasonally-averaged) data. The results shown are also diurnally-averaged (i.e. are averages over the 12 times of sol at which fields are stored in the MCD). The right-hand plots show the diurnally-averaged lifted dust flux, predicted using the GST parameterization, and given in arbitrary units since the exact values depend on the choice of the lifting efficiency $\alpha_N$ (which relates dust flux to sand flux via Eqn. 10). The sand flux, predicted by assuming a gustiness parameter $\kappa$=1.5, is first found at each of the 12 times of sol for which the MCD provides wind magnitudes and other necessary input variables, and is then averaged to give a diurnal average. The threshold values used (not shown) are dominated by a large inverse surface pressure signal, hence are highest over Tharsis, lowest over Hellas, and are calculated using Eqns. 5 – 8 with $I_{\mathrm{p}}$=1×10$^{-7}$Nm$^{-1/2}$ and the saltating particle diameter set to 60$\mu$m.

Considering first the results for season 10 (southern summer), the clearest feature is the strong summer hemisphere westerlies at about 30°S, with the most easterly winds centered on or just north of the equator. The latitude of the strongest westerlies corresponds roughly to that of the rising branch of the single, cross-equatorial Hadley cell which exists on Mars at this time (see e.g. *Haberle et al.* [1993] for further discussion). The gross surface wind pattern produced is a result of angular momentum conservation within the near-surface (north to south) branch. *Forget et al.* [1999] discuss in more detail the zonal-mean dynamics of the AOPP-LMD Mars general circulation model, and show zonally-averaged fields corresponding to seasons 1, 4, 7 and 10 (including mass stream function and angular momentum for season 10). The circulation is generally about half as strong during northern summer as during southern summer, largely because of the eccentricity of Mars's orbit which leads to the southern hemisphere receiving ∼40% more solar insolation during its summer period, but also due to the cross-equatorial slope in zonal-mean topography (*Joshi et al.* [1995], *Richardson and Wilson* [2002]) and to dynamical feedbacks which reinforce the effect of these asymmetries (e.g. *Zurek et al.* [1992]).

The mean meridional circulation cannot account for the zonally asymmetric surface wind patterns predicted by the model and observed on Mars, for example, the strong meridional

**Near−surface drag velocities and wind vectors (m/s)**

**GST NSWS lifted dust flux (arbitrary units)**

**Season 1**
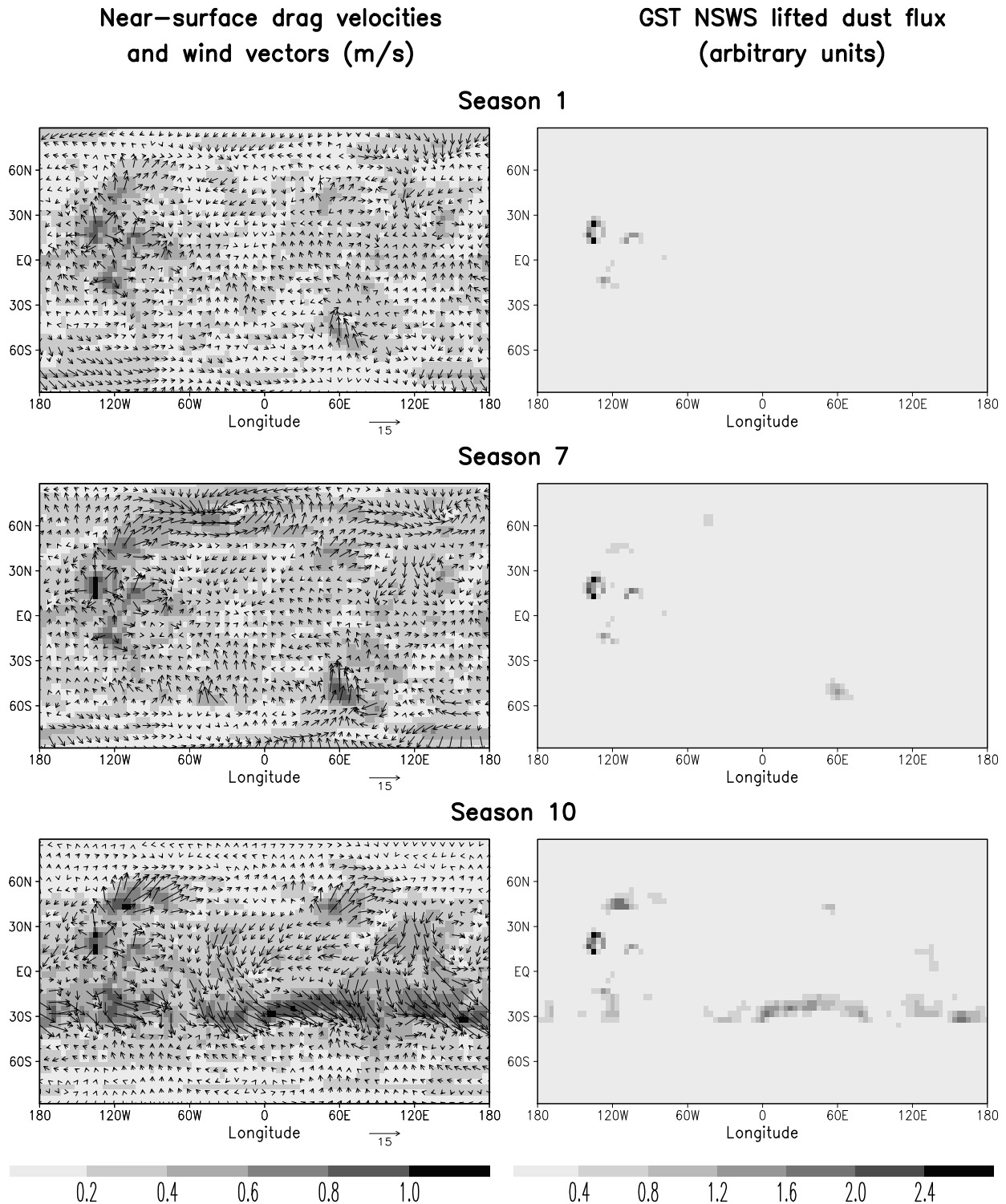


**Season 7**



**Season 10**



Figure 2: The left-hand plots show near-surface drag velocity (shading) and wind vectors (arrows). The right-hand plots show the dust flux lifted using the GST parameterization. Results are for seasons 1, 7 and 10 using MCD Viking dust scenario data.

velocities to the east of the Tharsis ridge and again to the east of Syrtis Major. These are concentrations of the Hadley cell's low level return flow to the western sides of basins, and are known as western boundary currents (see e.g. *Joshi et al.* [1995] for further explanation).

There are also more localized maxima in wind magnitude around the Tharsis peaks, and around the Hellas basin. These are predominantly anabatic (daytime upslope) and katabatic (nighttime downslope) winds, driven by the horizontal temperature gradients resulting from heating over slopes (e.g. *Savijärvi and Siili* [1993]). Other strong circulations or thermal contrast flows include those at the boundary between ice cover and regolith. At high latitudes in particular there is significant turning of these local flows by the Coriolis effect, and they may also combine to enhance or reduce each other. Unlike winds associated with the general circulation, these local flow regimes often decrease in strength as dust levels increase (e.g. due to the dust lifting they themselves cause), since a dustier atmosphere tends to have reduced thermal contrasts. This negative feedback on dust lifting is a possible mechanism for self-shut down of dust storms initiated by such flows.

During the other two seasons shown in Fig. 2, during northern (season 1) and southern (season 7) spring, there are two Hadley cells present, rising over equatorial regions and descending in mid-latitudes, and at these times there are generally far weaker surface winds, with local regimes (such as slope winds around the Tharsis peaks and Hellas) now dominating.

### 4.1.2 Dust lifting using GST

The patterns of dust lifting using the GST parameterization closely reflect the seasonal patterns of wind velocity. There is a prominent band of strong lifting within a zonal collar centered at 30°S in season 10, which generally peaks between the hours of 11am and 5pm local time. There is also peak lifting in all seasons around the Tharsis peaks, greatest between about 8pm and 8am local time around Olympus Mons, with the downslope winds there reaching maximum velocities just before dawn. The exact relationship between drag velocity and dust lifted is of course determined by the threshold values, but to a large extent to know the pattern of drag velocity is to have a good idea of the pattern of dust lifting. Particularly interesting is the peak in lifting within the Hellas basin during season 7, which is absent in season 10. This is due to a particularly strong local wind regime during southern spring when the southern Hellas slopes are still ice-covered (resulting in downslope winds during night and day, allowing stronger flows to develop, see e.g. *Siili et al.* [1999]). Additionally the condensation-sublimation flow is off-cap, and low temperatures also result in low threshold drag velocities (which decrease as density increases), hence the large peak in lifting here. This has disappeared by season 10 by which time the slopes are ice free, and the increased dust levels at this time of year (using the Viking dust scenario) also reduce thermal contrasts near the surface. It should be noted that in full DMGCM simulations dust lifting is not allowed where the surface is ice-covered, but strong downslope flows over ice-covered slopes

may still enhance wind stresses over adjacent ice-free regions.

Finally, it is important to note that there is some GST lifting predicted at every grid-point, albeit very little in many cases. This reflects the lack of an upper limit on the integration over the Weibull probability density function, described in section 3.1.3, which results in some lifting occurring even when the drag velocity obtained from the MCD is vastly below threshold. There are therefore no cut-offs, and generally there is in fact a very smooth spatial variation in the amount of lifting.

### 4.1.3  Dust lifting using NOG

Unlike GST results, in NOG lifting the thresholds play an important role in restricting dust injection to only a few grid-points and times when conditions are exceptionally favorable. Results using the threshold-sensitive NOG parameterization are not shown here, but consist of lifting almost only predicted around the Tharsis peaks, where slope winds are highest. The lifting is marginally greatest during season 10, mostly owing to lower thresholds around Tharsis and Elysium caused by a colder, denser near-surface atmosphere (see Eqn. 5). A more detailed examination of the results shows that the closest this experiment comes to producing lifting in the southern hemisphere is during season 7, when drag velocities approach the threshold values on the southern slopes of Hellas.

## 4.2  Lifting by dust devils

### 4.2.1  Contributing variables

Surface to air temperature difference and thermodynamic efficiency are the most important factors in determining lifting by both the DTH and DDA dust devil lifting parameterizations described in section 3.2, as these determine the basic strength of the dust devils which may form. The top row of plots in Fig. 3 shows the surface to level 1 air temperature difference, and the second row the thermodynamic efficiency, at three times of sol in season 10 (northern hemisphere winter) using Viking dust scenario MCD data. Level 1 here is the lowest model level, typically at ∼5m above the surface. The temperature difference broadly indicates the energy available to drive any dust devils which may form, and a diurnal cycle is prominent, with the peak temperature difference following the path of the peak in solar insolation. The pattern is similar during other seasons, except that the distribution is centered furthest north during northern summer, and furthest south during southern summer, in line with the latitudinal variation of the sub-solar point. The magnitude of the temperature difference varies little with season, although is reduced slightly during southern summer when dust levels are greatest.

Thermodynamic efficiency increases with the depth of the convective boundary layer and relates to how high (and hence how large and strong) dust devils are able to grow. There

**Midnight at 0 longitude**    **8 am at 0 longitude**    **4 pm at 0 longitude**

**Surface − level 1 temperature (K)**



**Thermodynamic efficiency (arbitrary units)**



**Tangential velocity (m/s)**



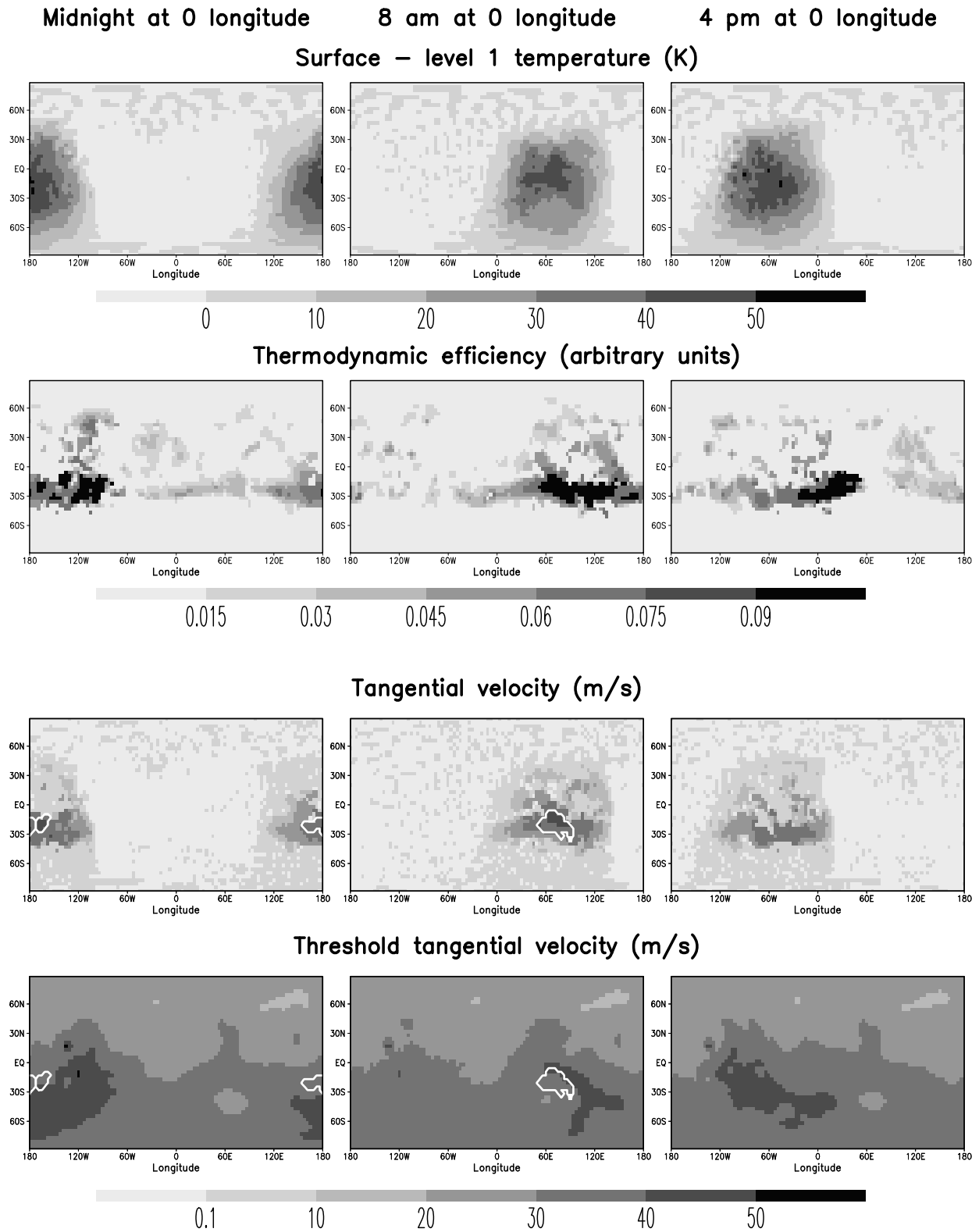**Threshold tangential velocity (m/s)**



Figure 3: The first row shows surface to air temperature differences and the second shows thermodynamic efficiencies in season 10, both used to predict dust devil lifting. The bottom two rows relate to DTH lifting (predicted to occur within the white contours), the third row showing tangential velocities and the fourth shows the threshold values required for lifting.

is also a diurnal cycle in this variable, now peaking slightly later in the day at about 2–4 pm local time, as a result of the time required to establish a strong convective boundary layer following the peak in instantaneous solar insolation at noon. During near-solstice seasons, the strong winds of the summer hemisphere subtropical jet are accompanied by high values of turbulent kinetic energy, resulting in a deeper convective boundary layer here which greatly increases the thermodynamic efficiency. Season 10 contains the peak values of thermodynamic efficiency, with these mostly restricted to a southern zonal collar centered on ∼30°S, i.e., the region of the subtropical jet. Efficiency is also increased over high terrain in the northern hemisphere (e.g. Tharsis, Syrtis Major and Elysium).

### 4.2.2 Dust lifting using DDA

DDA dust lifting (see section 3.2.3) is not represented in Fig. 3, but peak lifting areas are similar to those where thresholds are exceeded in the DTH parameterization (shown as white contours in the bottom two rows of plots), although they are surrounded by more areas of increasingly weaker lifting as distance to the main lifting latitudes increases. Even if a suitable threshold value of dust devil activity were used, however, such a modified DDA parameterization would not give identical results to DTH, as the latter has a greater dependence on the thermodynamic efficiency and no direct dependence on drag velocity.

### 4.2.3 Dust lifting using DTH

The threshold-sensitive DTH parameterization predicts lifting when the tangential velocity around a dust devil exceeds a threshold value (see section 3.2.3). The estimated tangential velocity depends on the size of the pressure drop across the dust devil vortex. This is related to both the surface to air temperature difference and thermodynamic efficiency (*Rennó et al.* [1998]), as demonstrated by the third row of plots in Fig. 3 which correlates with both rows above. The point at which the temperature difference becomes negative acts as one cut-off, preventing lifting in many regions despite high thermodynamic efficiencies, but a second cut-off is provided by the threshold tangential velocity. This is shown in the lowest row of plots, and acts to partially compensate for the high values of $v_{\text{tang}}$ over topography (as thresholds are highest here also). Regions where thresholds are exceeded (and hence DTH lifting is predicted to occur) lie within the white contours marked on the bottom two rows of plots. DTH lifting is thus restricted to relatively narrow bands of latitude, and with regard to zonal variation peaks in the region 120°–180°E in season 10. The seasonal variation of lifting is very similar to that of thermodynamic efficiency, with for example peak lifting in season 10, less in season 4, very little in season 1 and none in season 7.

## 4.3 The effect of increased dust opacity on predicted dust lifting

Figure 4 shows the impact of gross changes in atmospheric dustiness on predicted dust fluxes using the two threshold-insensitive parameterizations, GST and DDA. The results serve to indicate the likely overall feedbacks on lifting by both mechanisms, since increased global dustiness is a consequence of dust lifting (as is a local opacity increase in the immediate vicinity of the lifting region). The left-hand plots show GST lifting, with opacity increasing from top to bottom. There is a clear shift from lifting dominated by local wind regimes to lifting controlled by general circulation wind patterns as opacity increases. As the dust content of the atmosphere increases so does the strength of the Hadley cell, which responds to greater and more vertically extended solar heating, and the associated near-surface winds (particularly the southern mid-latitude westerlies) increase also. Stronger thermal tides also force the circulation more – the semi-diurnal tide, for example, has a significant high-latitude response to strong dust heating, which results in the formation of a high summer latitude reverse cell, leading to large near-surface winds at about 70°S (as shown in the bottom left plot). At the same time, the more isothermal near-surface atmosphere leads to a reduction in slope winds and thermal contrast flows (e.g. around Tharsis). Overall, however, dust lifting strongly increases with atmospheric opacity, suggesting that on a global scale the near-surface wind stress mechanism has a strong positive feedback, as suggested by *Leovy et al.* [1973]: dust lifting increases atmospheric opacity, which in turn leads to a stronger circulation and stronger near-surface winds, so causing an increase in dust lifting in most regions, and so on.

The potential feedback effect of non-uniform dust loading, with discrete dust clouds, is not revealed by these experiments and must be examined using radiatively active dust transport in the DMGCM. Such experiments show that there is a strong positive feedback on near-surface wind stress lifting at the edge of dust clouds, where temperature gradients and hence winds are strongest, promoting increased dust lifting. Within a sufficiently opaque cloud, however, a near-surface region may become so isothermal that winds aloft are decoupled from those near the surface, shutting off lifting until the cloud has dissipated. This 'stabilization' effect has been suggested as a mechanism for dust storm decay (e.g. *Pollack et al.* [1979]), although DMGCM results indicate that exceptionally concentrated dust amounts are required for this to occur, exceeding even those found during the peak of global storms. This is discussed further in the companion paper (*Newman et al.* [2002]).

By contrast, the right-hand plots of Fig. 4 show that for DDA the trend is opposite to that for GST lifting, with a reduction in DDA lifting as dustiness is increased. This is a consequence of the reduced vertical temperature gradients near the surface, and in most of the boundary layer, with increased atmospheric dust heating. Increased opacity results in greater heating above the surface, with less radiation reaching the surface itself, which combine to reduce the surface to air temperature gradient thus lessening the energy available
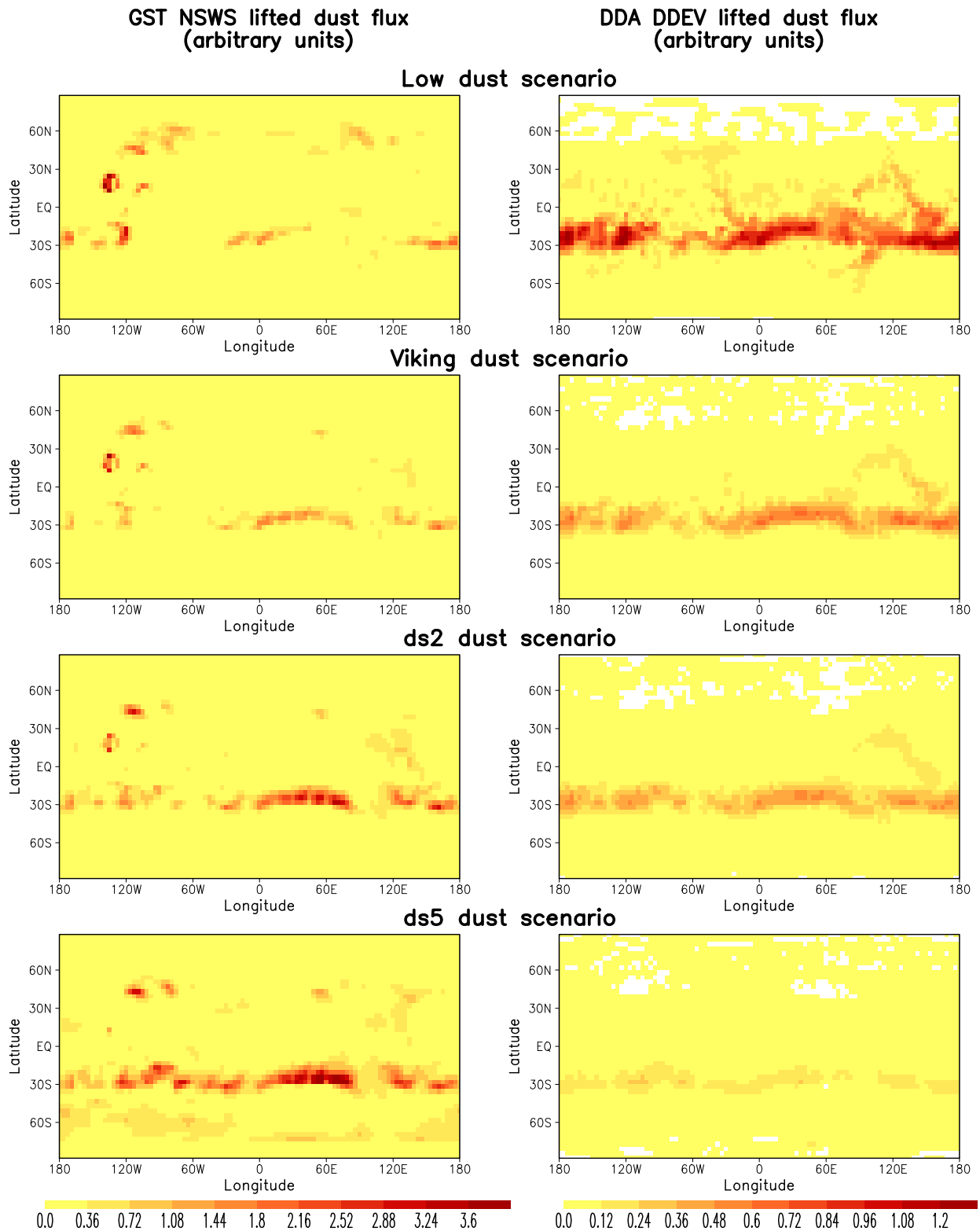
Figure 4: Dust lifting predicted in season 10 by the GST (left) and DDA (right) parameterizations for four different prescribed dust scenarios. All results were obtained using MCD data.

to drive dust devils at the ground. The effect on convective boundary layer thickness is more complex, as it depends on the vertical distribution of heating from the surface upwards. It is greatest for the low dust scenario, which has an atmospheric dust opacity of only 0.1 in the visible and a low dust top, so allows a strong convective boundary layer to form above the well-heated surface. The convective boundary layer thickness decreases greatly in Viking scenario results, owing to dust being distributed through a thicker vertical layer which results in a more even distribution of heating and increased stability. The convective boundary layer thickness increases slightly in some areas from the Viking to ds2 and ds5 simulations, mostly in regions where near-surface wind velocities and hence turbulent kinetic energies are greatly increased. Overall, however, dust lifting strongly decreases with atmospheric opacity, suggesting that the dust devil lifting mechanism has a strong negative feedback: dust lifting increases atmospheric opacity, which in turn leads to reduced thermal contrasts in the near-surface atmosphere, so causing a decrease in the energy available to drive and maintain dust devils and hence decreasing dust lifting.

# 5 Parameterized dust lifting experiments with radiatively active dust transport

Section 4 described the results of experiments without radiatively active dust transport, using seasonally-averaged data from the MCD. These results, and the inferences made regarding the likely direction of feedbacks on each mechanism, are restricted in that the lifted dust did not affect the atmospheric state, and hence did not affect further lifting. The following results are obtained using the DMGCM with radiatively active dust transport to determine whether or not the suggested feedbacks actually occur, and to investigate whether the pattern of dust lifting is affected.

## 5.1 Dust lifting feedbacks

Figure 5 shows the total dust mass in the atmosphere throughout three radiatively active dust transport DMGCM simulations, using the GST (top) and DDA (bottom) lifting parameterizations. These experiments use different lifting efficiencies (respectively $\alpha_N$ or $\alpha_D$), with the range of peak zonally-averaged visible dust opacities produced varying from 0.35 for ZD5A to 2.15 for ZD7A, and from 0.25 for ZN5A to 15.5 (more than double peak observed values) for ZN7A. In each case the mass is shown divided by the lifting efficiency used (therefore if no feedbacks were present the lines would simply overlay each other). In each plot, the result of using radiatively inactive dust transport in a Viking dust scenario simulation is also shown for comparison. If near-surface wind stress lifting has positive and dust devil lifting negative feedbacks, increasing $\alpha_N$ for GST lifting should increase the weighted dust mass,

but increasing $\alpha_D$ for DDA lifting should decrease the weighted dust mass. This is found to be the case overall, and the feedbacks (in this case positive) are seen to be particularly strong for GST lifting. The total dust mass is multiplied by more than 5 times when $\alpha_N$ is increased by a factor of 5, but is multiplied by almost 100 times when $\alpha_N$ is increased by a factor of 10. The variation of dust mass through the year using threshold-insensitive lifting is clearly linked to the seasonal cycle, with a peak during southern summer for GST and DDA, and a secondary maximum in northern summer for DDA.

## 5.2 Patterns of dust lifting

Figure 6 provides an overview of the pattern of dust lifting from the surface in year-long radiatively active dust transport simulations using the two near-surface wind stress parameterizations (GST and NOG) and the two dust devil parameterizations (DDA and DTH). The GST experiment uses $I_\mathrm{p}{=}5{\times}10^{-7}\mathrm{Nm}^{-1/2}$ whereas the NOG experiment uses both a lower interparticle cohesion, $I_\mathrm{p}{=}1{\times}10^{-7}\mathrm{Nm}^{-1/2}$, and a higher lifting efficiency, $\alpha_N$, to compensate for the reduced lifting in the absence of any assumed gustiness. Each plot shows the dust lifted at each grid-point averaged over the entire year, and normalized by the planet-wide average. The first clear result is that the bulk of the lifting is far more confined to a few grid-points in the threshold-sensitive parameterizations NOG and DTH. In NOG, for example, one Tharsis grid-point represents 130 times the average grid-point lifting over the whole planet, and the lifting is most evenly spread for the DDA parameterization.

Considering the two near-surface wind stress parameterizations, both show lifting peaks around Hellas, Elysium, Tharsis and Alba Patera. Using the NOG parameterization lifting is zero almost everywhere else, excepting small amounts raised in Argyre, in some areas around the northern cap edge, and within western boundary currents. The DTH parameterization similarly has far more areas with zero lifting than DDA (which has none when averaged over a year). DDA lifting peaks within a zonal collar from $\sim$15°–30°S during southern summer, greatest within the longitude ranges $\sim$140°–100°W (Thaumasia/Solis), $\sim$40°–20°W (Margaritifer Sinus), $\sim$90°E (Mare Tyrrhenum) and $\sim$120°–160°E (Hesperia/Mare Cimmerium), and within a slightly more equatorwards zonal collar of northern latitudes during northern summer, peaking at $\sim$120°W (Tharsis) and $\sim$70°E (just west of Syrtis Major). DTH shares many of the same areas, but peaks in the southern hemisphere at $\sim$0° (Noachis/Deucalionis) and 150°–180°E (Mare Cimmerium), and in the northern hemisphere in the range $\sim$190°–150°W (Amazonis) and, as before, at $\sim$70°E.

In these simulations the atmospheric variables required to predict dust lifting at each timestep are fully consistent with prior lifting, and this affects most strongly the distribution of dust devil lifting. This is particularly noticeable using the DTH parameterization, where lifting is most confined to the regions of peak surface to air temperature difference and convective boundary layer height. The latter tends to shift position as the atmospheric dust
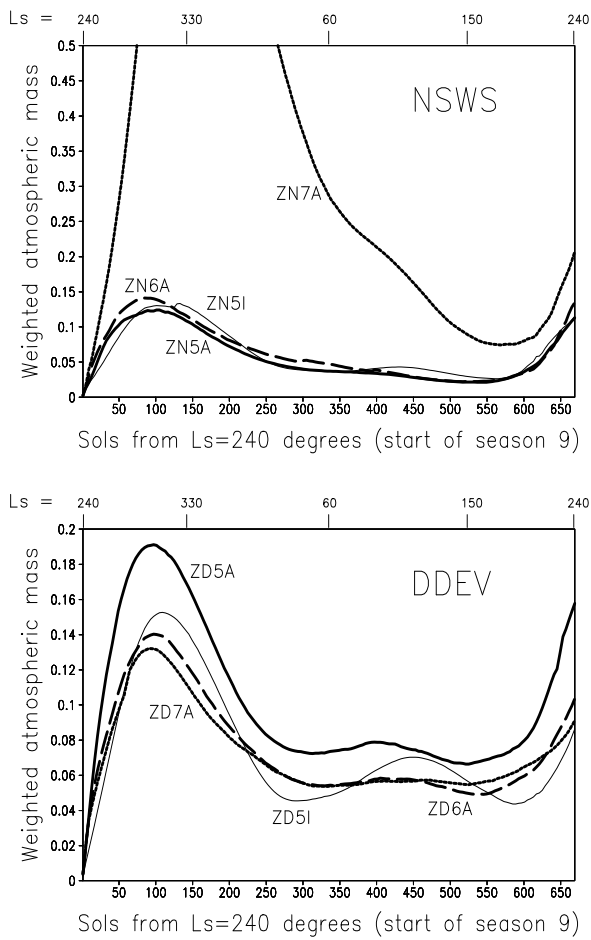
Figure 5: Top: mass totals, divided by the $\alpha_N$ value used, for year-long DMGCM simulations using GST (threshold-insensitive near-surface wind stress) lifting. ZN5A, ZN6A and ZN7A are radiatively active simulations with $\alpha_N$ in the ratio 1:5:10, and ZN5I is a radiatively inactive version of ZN5A. Bottom: similar but for DDA (threshold-insensitive dust devil) lifting with $\alpha_D$ values in the ratio 1:5:10.
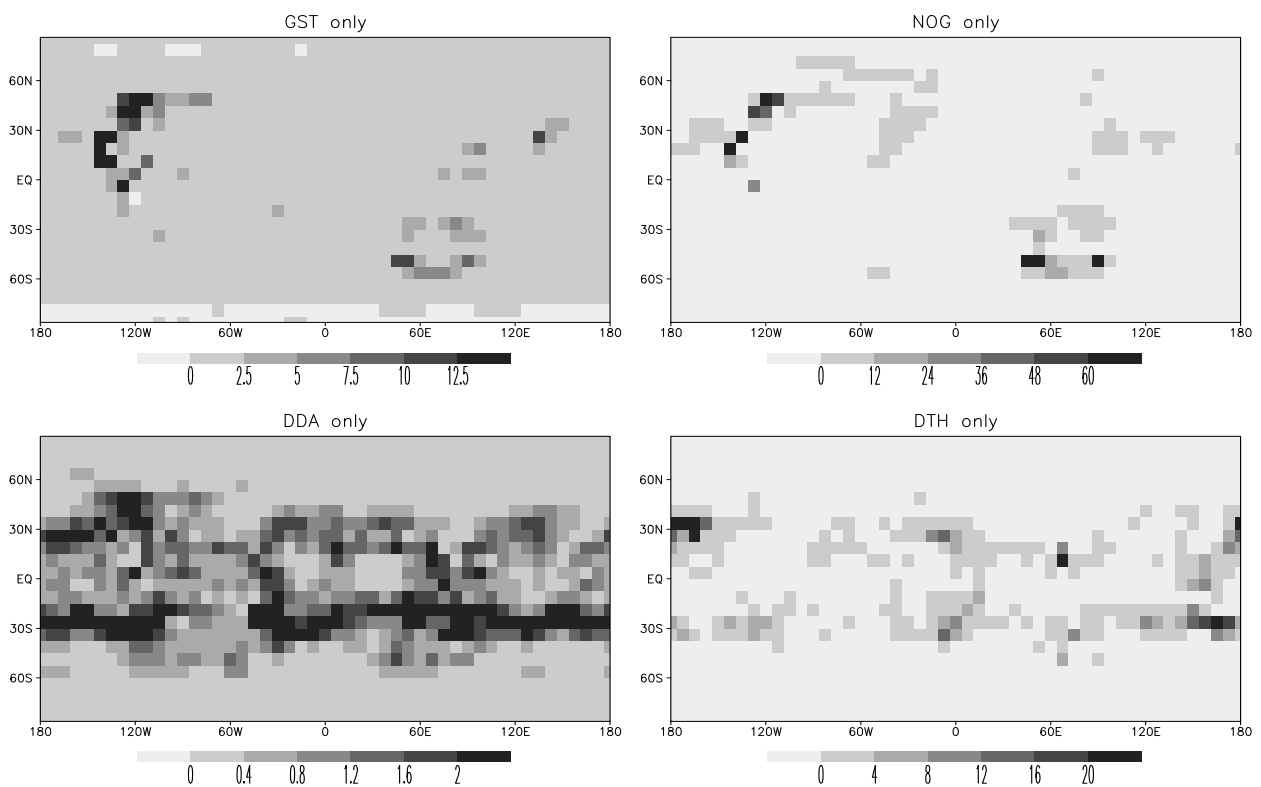
Figure 6: The pattern of dust lifting in year-long radiatively active dust transport DMGCM simulations using the two near-surface wind stress parameterizations, GST (threshold-insensitive) and NOG (threshold-sensitive), and the two dust devil parameterizations, DDA (threshold-insensitive) and DTH (threshold-sensitive). Each plot shows the dust lifting per output time-step at each grid-point, averaged over the entire year, and normalized by the planet-wide average.

distribution interacts with the atmospheric state, resulting in the formation of a zonally asymmetric dust distribution. The net result is a shift from peak DTH lifting occurring at ~120°E in a passive, to occurring at ~0° and 180° in a radiatively active, dust transport experiment.

## 5.3 Dust lifting compared with observations

### 5.3.1 Storm onset locations

Figure 7 shows the frequency of observed dust cloud activity during the early stages of large storms from ~1894–1990 (using data compiled by *Martin and Zurek* [1993]). Each dot represents one observation of likely dust raising activity (although it is possible that in some cases a cloud persisted in an area without lifting actually occurring there). The near-surface wind stress lifting predictions match some locations, for example the western and eastern slopes of Hellas, and to some extent the slopes of Argyre and the northern Chryse region (which show up as secondary peaks in NOG results), but fail to reproduce the Hellespontus, Noachis or Thaumasia/Solis maxima. This parameterization also predicts far more lifting over Tharsis than is represented in these observations, but this may be due to such lifting not usually forming the initial clouds of a large storm event, since the dust is generally not transported far before being redeposited.

The dust devil lifting predictions show less lifting within Hellas and Argyre (generally peak lifting is limited to regions between 40°S and 40°N), but there is more lifting within the Noachis region (particularly for DTH), Thaumasia/Solis (particularly for DDA) and near Syrtis Major. Lifting over Tharsis is also reduced, but two prominent lifting areas, 150°–180°E at 30°S, and 180°–120°W at 30°N, do not correlate with observations of initial major storm clouds (although the latter region has been noted as the site of frequent local dust storms, e.g. in recent Mars Global Surveyor Thermal Emission Spectrometer observations, *Smith et al.* [2001]).

### 5.3.2 Comparing near-surface wind stress lifting with dark streaks

Dark streaks are generally taken to be due to erosion of dust due to high wind stresses (revealing an underlying darker surface), hence a comparison of near-surface wind stress lifting predictions with global compilations of streak data (see e.g. *Thomas et al.* [1984], *Kahn et al.* [1992]) provides a more direct means of validation for this mechanism. The comparison with Fig. 2, which shows predicted dust lifting using the GST parameterization in seasons 1, 7 and 10, is quite good. In particular the zonal collar of high dust lifting from ~15°–35°S shows up clearly in streak observations, as does the lifting induced by topographic winds (over Tharsis and Alba Patera, and on the slopes of Hellas and Argyre). An observed
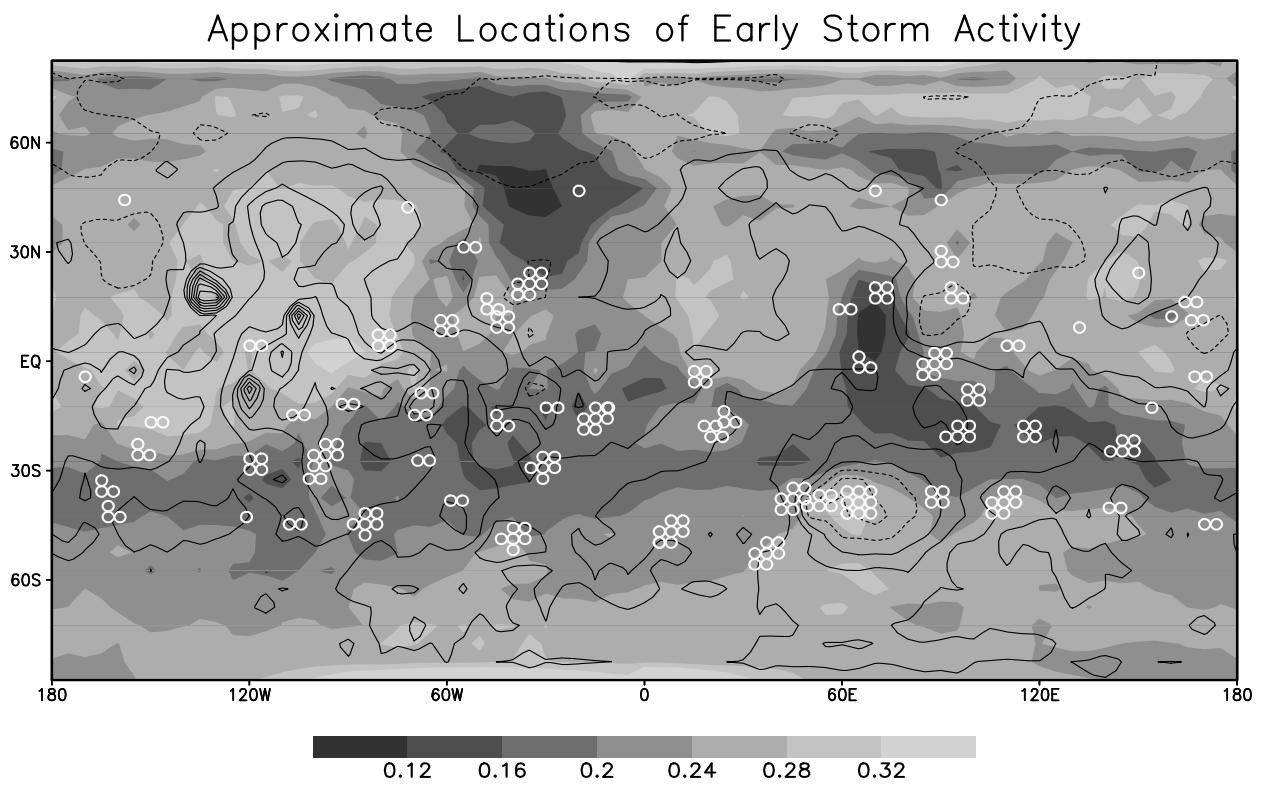
## Approximate Locations of Early Storm Activity



Figure 7: Approximate locations of early dust activity during onset of large Martian dust storms (data taken from a compilation by *Martin and Zurek* [1993]). Also shown is height above the reference geoid (contours are every 2km and negative values are shown as dashed lines) and albedo (shading).

clump of streaks over Noachis is not reproduced in lifting predictions, however, which suggests that possibly surface roughness is greater in this region, or interparticle cohesion less, thereby allowing more near-surface wind stress lifting to occur here on Mars itself than in the model.

### 5.3.3 Comparing dust devil lifting with dust devil streaks and clouds

A direct comparison between dust devil lifting predictions and observations of dust devil events is made difficult by the sparseness of images obtained at sufficient resolution to detect these vortices. No global maps of dust devil occurrence are currently available, but recent MOC images (*Edgett and Malin* [2000b]) have shown them to occur in nearly every environment where imaging has allowed a search for the narrow, dark streaks, with rapid changes in direction, which signify their passage. The bright, columnar dust devil clouds themselves have also been detected in these MOC images, as well as in images taken by MPF (*Metzger and Carr* [1999]), having been first detected by the Viking orbiters (*Thomas and Gierasch* [1985]), when they were found in 3 sols out of the 5 sols during which Arcadia Planitia ($\sim$33°–43°N, 148°–160°W) was observed at high resolution. This corresponds well with the peak in dust devil lifting predicted here (see Fig. 6). *Ryan and Lucich* [1983] used atmospheric measurements made by Viking Lander 1 and 2 to infer the presence of dust devils over the lander sites (respectively 48.0°W, 22.5°N and 134.3°E, 48.0°N). They found that most occurred during spring and summer, consistent with the variation of dust devil lifting with season which is predicted using the DMGCM.

## 6  Conclusions

Two key issues for Mars are the prediction of climate and dust storm activity, with the latter contributing greatly to the former's variability. Both therefore require the factors controlling the observed Martian dust cycle and its variability to be well understood, and to be correctly represented in the models used to perform simulations. The results described above are a first step towards the complete, autonomous modeling of Martian dust transport in the DMGCM, and address the important question of how, when and where dust is raised into the atmosphere. The main conclusions are summarized below.

1. The assumption of saltation-induced dust lifting appears to be required to account for the quantity and dominance of $\sim\mu$m-sized dust particles in the Martian atmosphere.

2. Results are dramatically affected by the use of a more threshold-sensitive parameterization. In the NOG parameterization, for example, lifting is cut off when winds fall below threshold, whereas in GST it merely declines, resulting in smooth spatial and temporal variations in lifting. The greatest lifting is also linked to seasonal rather than local wind regimes for GST. Seasonally high wind stresses may result in lower lifting peaks, but averaged over a

season the total dust raised exceeds that raised by local high wind regimes, which are generally far more confined in time and space. In NOG lifting, thresholds may be high enough that only lifting by local high wind regimes occurs. The local wind regimes are often reduced in dustier conditions, providing an effective self-shut down mechanism. Interannual variability may also be expected to increase, since the extreme conditions required to trigger storms in high threshold runs are likely to be more variable in time and space than seasonal wind patterns. For example, strong downslope flows in southern Hellas may produce far less lifting in a given year if the main contributing grid-points remain ice-covered for even a few sols longer. Threshold-sensitive lifting may therefore be vital to producing both shut-down of dust storms during the storm season and the observed degree of interannual variability, due to the reduced tie to the seasonal cycle of insolation and increased dependence on transient local high wind regimes.

3. Results indicate that near-surface wind stress lifting has strong, large-scale positive feedbacks, and that dust devil lifting has negative feedbacks.

4. In preliminary radiatively active dust devil lifting experiments the locations of peak lifting are found to vary from those in inactive runs, as transport feedbacks lead to the formation of zonally asymmetric atmospheric dust distributions, affecting heating rates, convective boundary layer heights and hence dust devil lifting.

5. Substantial correspondence is found between areas of peak predicted dust lifting and observed early storm activity, such as Hellas, or regions to the east of Syrtis Major and Tharsis where strong western boundary currents exist. Lifting predicted over Tharsis is not represented in the observations, but much of this occurs during southern summer, when dust lifted in the north is either rapidly redeposited or transported south so does not result in storm formation locally. The lack of predicted lifting in Noachis is more problematic, as the observed numbers of dark streaks here suggest that initial storm clouds over Noachis are indeed caused by the wind stress lifting mechanism. DDA lifting results match observations of early storm activity in the Hellas, Argyre, Noachis, Syrtis and Chryse regions, although also predict strong lifting in areas not reflected in observations. DTH results also match observations of storm activity in Hellas, Noachis and Syrtis, but show little lifting around Argyre (a frequent storm onset region), and strong peaks in Mare Cimmerium and Amazonis/Arcadia ($\sim$180°W –150°W, 15°N –45°N) where initial major storm clouds are rarely observed. Dust devils and local storms are commonly observed in the latter region, suggesting that the parameterization is performing correctly but that these events do not generally develop into large storm clouds, perhaps because the dust is rapidly re-deposited.

The companion paper (*Newman et al.* [2002]) presents results from multi-annual radiatively active dust transport simulations with parameterized dust lifting, used to investigate the mechanisms responsible for the observed dust cycle. A major problem is the lack of observational and theoretical constraints on the lifting parameters, in particular the lifting

efficiencies, $\alpha_N$ and $\alpha_D$, without which there is great uncertainty in how the amount of near-surface wind stress lifting relates to that by dust devils. The situation would be greatly improved even if, for example, only $\alpha_D$ for DDA or DTH were known, as a simulation could then be performed using dust devil lifting only and a comparison with observations used to assess whether this mechanism alone is sufficient, or whether another must contribute.

Knowledge of $I_p$ is also highly desirable to estimate typical threshold values, although even with such data problems would remain. The NOG parameterization is, for example, too threshold-sensitive, and the GST parameterization probably overestimates the amount of lifting by near-surface wind stress. This suggests that an intermediate parameterization may be more correct, such as one similar to GST but with an upper limit placed on the size of wind gusts. With regard to dust devil lifting, the DDA parameterization is probably too threshold-insensitive, which could be addressed by introducing a lower limit of dust devil activity, below which the lifted dust flux would be set to zero.

### Acknowledgments

# References

[1] Alfaro, S. C., and L. Gomes, Modeling mineral aerosol production by wind erosion: Emission intensities and aerosol size distributions in source areas, *J. Geophys. Res.*, *106*, 18,075–18,084, 2001.

[2] Anderson, F. S., R. Greeley, P. Xu, E. Lo, D. G. Blumberg, R. M. Haberle, and J. R. Murphy, Assessing the Martian surface distribution of aeolian sand using a Mars general circulation model, *J. Geophys. Res.*, *104*, 18,991–19,002, 1999.

[3] Bagnold, R. A., *The Physics of Blown Sand and Desert Dunes*, Methuen, 1954.

[4] Balme, M., R. Greeley, B. Mickelson, J. Iversen, G. Beardmore, and S. Metzger, A laboratory scale vortex generator for simulation of Martian dust devils, in *American Geophysical Union, Fall Meeting 2001*, P31A-0542, 2001.

[5] Businger, J. A., J. C. Wyngaard, Y. Izumi, and E. F. Bradley, Flux-profile relationships in the atmospheric surface layer, *J. Atmos. Sci.*, *28*, 181–189, 1971.

[6] Carrol, J. J., and J. A. Ryan, Atmospheric vorticity and dust devil rotation, *J. Geophys. Res.*, *75*, 5179–5184, 1970.

[7] Clancy, R. T., and S. W. Lee, A new look at dust and clouds in the Mars atmosphere: analysis of emission-phase-function sequences from global Viking IRTM observations, *Icarus*, *93*, 135–158, 1991.

[8] Edgett, K. S., and M. C. Malin, New views of Mars eolian activity, materials, and surface properties: Three vignettes from the Mars Global Surveyor Mars Orbiter Camera, *J. Geophys. Res.*, *105*, 1623–1650, 2000a.

[9] Edgett, K. S., and M. C. Malin, Martian dust raising and surface albedo controls: Thin, dark (and sometimes bright) streaks and dust devils in MGS MOC high resolution images, 2000b, conference paper (Lunar and Planetary Science, XXXI).

[10] Forget, F., Improved optical properties of the Martian atmospheric dust for radiative transfer calculations in the infrared, *Geophys. Res. Lett.*, *25*, 1105–1109, 1998a.

[11] Forget, F., F. Hourdin, C. Hourdin, and O. Talagrand, Simulation of dust lifting and transport with the LMD mars general circulation model, in *Bull. Am. Astron. Soc.*, vol. 30, p. 1023, 1998b.

[12] Forget, F., F. Hourdin, F. Fournier, C. Hourdin, O. Talagrand, M. Collins, S. R. Lewis, P. L. Read, and J.-P. Huot, Improved general circulation models of the Martian atmosphere from the surface to above 80 km, *J. Geophys. Res.*, *104*, 24,155–24,175, 1999.

[13] Garratt, J. R., *The Atmospheric Boundary Layer*, Cambridge University Press, 1994.

[14] Gillette, D. A., B. Marticorena, and G. Bergametti, Change in the aerodynamic roughness height by saltating grains: Experimental assessment, test of theory, and operational parameterization, *J. Geophys. Res.*, *103*, 6203–6209, 1998.

[15] Greeley, R., and J. D. Iversen, *Wind as a Geological Process on Earth, Mars, Venus, and Titan*, Cambridge University Press, 1985.

[16] Greeley, R., N. Lancaster, S. Lee, and P. Thomas, Martian aeolian processes, sediments, and features, in *Mars*, chap. 22, pp. 730–766, The University of Arizona Press, 1992.

[17] Haberle, R. M., J. B. Pollack, J. R. Barnes, R. M. Zurek, C. B. Leovy, J. R. Murphy, H. Lee, , and J. Schaeffer, Mars atmospheric dynamics as simulated by the NASA Ames General Circulation Model 1. The zonal-mean circulation, *J. Geophys. Res.*, *98*, 3093–3123, 1993.

[18] Hess, G. D., and K. T. Spillane, Characteristics of Dust Devils in Australia, *J. Appl. Met.*, *29*, 498–507, 1990.

[19] Hourdin, F., and A. Armengaud, On the use of finite volume methods for atmospheric advection of trace species: I. test of various formulations in a general circulation model, *Tech. rep.*, Laboratoire de Météorologie Dynamique du Centre National de la Recherche Scientifique (CNRS), Paris, 1997.

[20] Hourdin, F., P. L. Van, F. Forget, and O. Talagrand, Meteorological variability and the annual surface pressure cycle on Mars, *J. Atmos. Sci.*, *50*, 3625–3640, 1993.

[21] James, P. B., and N. Evans, A local dust storm in the Chryse region of Mars: Viking orbiter observations, *Geophys. Res. Lett.*, *8*, 903–906, 1981.

[22] Joseph, J. H., W. J. Wiscombe, and J. A. Weinman, The delta-Eddington approximation for radiative flux transfer, *J. Atmos. Sci.*, *33*, 2452–2459, 1976.

[23] Joshi, M. M., S. R. Lewis, P. L. Read, and D. C. Catling, Western boundary currents in the Martian atmosphere: Numerical simulations and observational evidence, *J. Geophys. Res.*, *100*, 5485–5500, 1995.

[24] Joussaume, S., Three-dimensional simulations of the atmospheric cycle of desert dust particles using a general circulation model, *J. Geophys. Res.*, *95*, 1909–1941, 1990.

[25] Kahn, R. A., T. Z. Martin, R. W. Zurek, and S. W. Lee, The Martian dust cycle, in *Mars*, chap. 29, pp. 1017–1053, The University of Arizona Press, 1992.

[26] Leovy, C. B., R. W. Zurek, and J. B. Pollack, Mechanisms for Mars dust storms, *J. Atmos. Sci.*, *30*, 749–762, 1973.

[27] Lewis, S. R., M. Collins, P. L. Read, F. Forget, F. Hourdin, F. Fournier, C. Hourdin, O. Talagrand, and J.-P. Huot, A climate database for Mars, *J. Geophys. Res.*, *104*, 24,177–24,194, 1999.

[28] Lorenz, R. D., J. I. Lunine, J. A. Grier, and M. A. Fisher, Prediction of aeolian features on planets: Application to Titan paleoclimatology, *J. Geophys. Res.*, *100*, 26,377–26,386, 1995.

[29] Lorenz, R. D., J. I. Lunine, J. A. Grier, and M. A. Fisher, Martian surface wind speeds described by the Weibull distribution, *J. Spacecraft*, *33*, 754–756, 1996.

[30] Lunt, D. J., The mineral dust cycle at the last glacial maximum and present day, Ph.D. thesis, The University of Reading, Department of Meteorology, 2001.

[31] Marticorena, B., and G. Bergametti, Modeling the atmospheric dust cycle: 1. design of a soil-derived dust emission scheme, *J. Geophys. Res.*, *100*, 16,415–16,430, 1995.

[32] Martin, L. J., and R. W. Zurek, An analysis of the history of dust activity on Mars, *J. Geophys. Res.*, *98*, 3221–3246, 1993.

[33] McKim, R. J., The dust storms of Mars, *J. Br. Astron. Assoc.*, *106*, 185–200, 1996.

[34] Mellor, G. L., and T. Yamada, Development of a turbulence closure model for geophysical fluid problems, *Rev. Geophys.*, *20*, 851–875, 1982.

[35] Metzger, S. M., and J. R. Carr, Dust devil vortices seen by the Mars Pathfinder camera, *Geophys. Res. Lett.*, *26*, 2781–2784, 1999.

[36] Murphy, J. R., The Martian atmospheric dust cycle: Insights from numerical model simulations, 1999, conference paper (The Fifth International Conference on Mars).

[37] Murphy, J. R., J. B. Pollack, R. M. Haberle, C. B. Leovy, O. B. Toon, and J. Schaeffer, 3-dimensional numerical simulation of Martian global dust storms, *J. Geophys. Res.*, *100*, 26,357–26,376, 1995.

[38] Newman, C. E., S. R. Lewis, P. L. Read, and F. Forget, Modeling the dust cycle in a Mars general circulation model. 2: Multi-annual radiatively active dust transport simulations, *J. Geophys. Res.*, 2002, this issue.

[39] Nickovic, S., G. Kallos, A. Papadopoulos, and O. Kakaliagou, A model for prediction of desert dust cycle in the atmosphere, *J. Geophys. Res.*, *106*, 18,113–18,129, 2001.

[40] Pollack, J. B., R. Haberle, R. Greeley, and J. D. Iversen, Estimates of the wind speeds required for particle motion on Mars, *Icarus*, *29*, 395–417, 1976.

[41] Pollack, J. B., D. S. Colburn, F. M. Flasar, R. Kahn, C. E. Carlston, and D. C. Pidek, Properties and effects of dust particles suspended in the Martian atmosphere, *J. Geophys. Res.*, *84*, 2929–2945, 1979.

[42] Pollack, J. B., M. E. Ockert-Bell, and M. K. Shepard, Viking lander image analysis of Martian atmospheric dust, *J. Geophys. Res.*, *100*, 5235–5250, 1995.

[43] Priestley, A., A quasi-conservative version of the semi-Lagrangian advective scheme, *Monthly Weather Rev.*, *121*, 621–629, 1993.

[44] Raupach, M., Saltation layers, vegetation canopies and roughness lengths, *Acta Mech.*, *1*, 83–96, 1991.

[45] Rennó, N. O., M. L. Burkett, and M. P. Larkin, A simple thermodynamical theory for Dust Devils, *J. Atmos. Sci.*, *55*, 3244–3252, 1998.

[46] Rennó, N. O., A. A. Nash, J. L. Lunine, and J. Murphy, Martian and terrestrial dust devils: Test of a scaling theory using Pathfinder data, *J. Geophys. Res.*, *105*, 1859–1865, 2000.

[47] Richardson, M. L., and R. J. Wilson, A topographically forced asymmetry in the Martian circulation and climate, *Nature*, *416*, 298–300, 2002.

[48] Rossow, W. B., Cloud microphysics: Analysis of the clouds of Earth, Venus, Mars and Jupiter, *Icarus*, *36*, 1–50, 1978.

[49] Ryan, J. A., Relation of Dust Devil frequency and diameter to atmospheric temperature, *J. Geophys. Res.*, *77*, 7133–7137, 1972.

[50] Ryan, J. A., and R. D. Lucich, Possible Dust Devils, vortices on Mars, *J. Geophys. Res.*, *88*, 11,005–11,011, 1983.

[51] Savijärvi, H., and T. Siili, The Martian slope winds and the nocturnal PBL jet, *J. Atmos. Sci.*, *50*, 77–88, 1993.

[52] Seguro, J. V., and T. W. Lambert, Modern estimation of the parameters of the Weibull wind speed distribution for wind energy analysis, *J. Wind Eng. Indust. Aerodyn.*, *85*, 75–84, 2000.

[53] Siili, T., R. M. Haberle, J. R. Murphy, and H. Savijärvi, Modelling of the combined late-winter ice cap edge and slope winds in Mars' Hellas and Argyre regions, *Plan. Space Sci.*, *47*, 951–970, 1999.

[54] Sinclair, P. C., The lower structure of Dust Devils, *J. Atmos. Sci.*, *30*, 1599–1619, 1973.

[55] Smith, M. D., J. C. Pearl, B. J. Conrath, and P. R. Christensen, Thermal Emission Spectrometer results: Atmospheric thermal structure and aerosol distribution, *J. Geophys. Res.*, *106*, 23,929–23,946, 2001.

[56] Sutton, J. L., C. B. Leovy, and J. E. Tillman, Diurnal variations of the Martian surface layer meteorological parameters during the first 45 sols at two Viking lander sites, *J. Atmos. Sci.*, *35*, 2346–2355, 1978.

[57] Tegen, I., and I. Fung, Modeling of mineral dust in the atmosphere: Sources, transport, and optical thickness, *J. Geophys. Res.*, *99*, 22,897–22,914, 1994.

[58] Thomas, P., and P. J. Gierasch, Dust devils on Mars, *Science*, *230*, 175–177, 1985.

[59] Thomas, P. C., J. Veverka, D. Gineris, and L. Wong, Dust streaks on Mars, *Icarus*, *60*, 161–179, 1984.

[60] Toon, O. B., J. B. Pollack, and C. Sagan, Physical properties of the particles comprising the Martian dust storm of 1971-1972, *Icarus*, *30*, 663–696, 1977.

[61] Toon, O. B., C. P. McKay, T. P. Ackerman, and K. Santhanam, Rapid calculation of radiative heating rates and photodissociation rates in inhomogeneous multiple scattering atmospheres, *J. Geophys. Res.*, *94*, 16,287–16,301, 1989.

[62] Westphal, D. L., O. B. Toon, and T. N. Carlson, A case-study of mobilization and transport of Saharan dust, *J. Atmos. Sci.*, *45*, 2145–2175, 1988.

[63] White, B. R., Soil transport by winds on Mars, *J. Geophys. Res.*, *84*, 4643–4651, 1979.

[64] Williamson, D. L., and P. J. Rasch, Two-dimensional semi-Lagrangian transport with shape-preserving interpolation, *Monthly Weather Rev.*, *117*, 102–129, 1989.

[65] Wilson, R. J., A general circulation model simulation of the Martian polar warming, *Geophys. Res. Lett.*, *24*, 123–126, 1997.

[66] Wilson, R. J., and K. Hamilton, Comprehensive model simulation of thermal tides in the Martian atmosphere, *J. Atmos. Sci.*, *53*, 1290–1326, 1996.

[67] Woodward, S., Modeling the atmospheric life cycle and radiative impact of mineral dust in the Hadley Centre climate model, *J. Geophys. Res.*, *106*, 18,155–18,166, 2001.

[68] Zurek, R. W., and L. J. Martin, Interannual variability of planet-encircling dust activity on Mars, *J. Geophys. Res.*, *98*, 3247–3259, 1993.

[69] Zurek, R. W., J. R. Barnes, R. M. Haberle, J. B. Pollack, J. E. Tillman, and C. B. Leovy, Dynamics of the atmosphere of Mars, in *Mars*, chap. 26, pp. 835–933, The University of Arizona Press, 1992.